

Impact on floating thin elastic sheets: Dynamic wrinkling is controlled by fluid inertia

Finn Box¹, Doireann O'Kiely¹, Ousmane Kodio¹, Maxime Inizan¹, Alfonso A. Castrejón-Pita², and Dominic Vella¹

¹*Mathematical Institute, University of Oxford, Oxford OX2 6GG, United Kingdom and*

²*Department of Engineering Science, University of Oxford, Oxford OX1 3PJ, United Kingdom*

(Dated: October 11, 2024)

We investigate the impact of a solid sphere onto an ultra-thin polymer sheet floating on water. The vertical deflection of the sheet's centre draws material radially inwards, and results in an orthoradial compression that is relieved by the wrinkling of the entire sheet. Here we show that this wrinkling is truly dynamic, exhibiting features that are qualitatively different to those seen in quasi-static wrinkling experiments. In particular, we show that the wrinkles coarsen dynamically, rather than exhibiting the refinement that has been reported in quasi-static experiments. This difference is due to the inhibiting effect of the fluid inertia, which also limits the region of the sheet that experiences a significant vertical deflection. As well as studying the wrinkling in detail, we suggest that the presence of such thin elastic sheets at interfaces may be an effective way of reducing the splash that might otherwise be observed.

Wrinkling provides a means of dramatically reconfiguring slender structures [1], and offers new opportunities for controlling and measuring materials in applications [2] from thin sheet metrology [3–5] to photonic devices [6, 7]. While the regular wavelength of a wrinkle pattern is perhaps its most aesthetically appealing feature, it is also key in such applications. Much work has therefore focussed on understanding static scenarios, where the wavelength is determined by energy minimization [4, 8–10]. The wrinkled state is interesting in its own right: the hierarchy of energies is somewhat delicate [9, 11] allowing thin sheets to waste excess length and, in so doing, attain energetically favourable states that would otherwise be inaccessible [12–14].

Perhaps the simplest experiment that reveals some of the complexity of wrinkling is the indentation of an ultra-thin elastic sheet floating at a liquid–air interface [5, 10, 12, 15, 16]. Indentation draws material radially inwards, in the process creating compressive stresses in the azimuthal direction. At a critical indentation, this compression overcomes the base capillary tension in the sheet [12], and radial wrinkles form. Beyond the indentation threshold, these wrinkles become more refined [10], increasing in number as the indentation depth increases, before deep folds form [15]. Here, we investigate how this static picture changes when indentation is performed dynamically, via impact.

Dynamic buckling instabilities have been investigated, among other things, as a route for inducing pattern formation in rigid objects [17–20] and understanding the fragmentation of brittle objects [21–23]. In particular, impact on an elastic sheet has been studied both for a sheet in free-fall [23] and a sheet floating on the surface of water [24, 25]; in both cases, a longitudinal tensile wave propagates outwards from the point of impact at the speed of sound, stretching the sheet, followed by a transverse wave that propagates through the stretched domain. A coupling between these two waves leads to an azimuthal compression that is analogous to that of static loading and again leads to wrinkling with a wrinkle wavelength that is fixed and may be understood using static

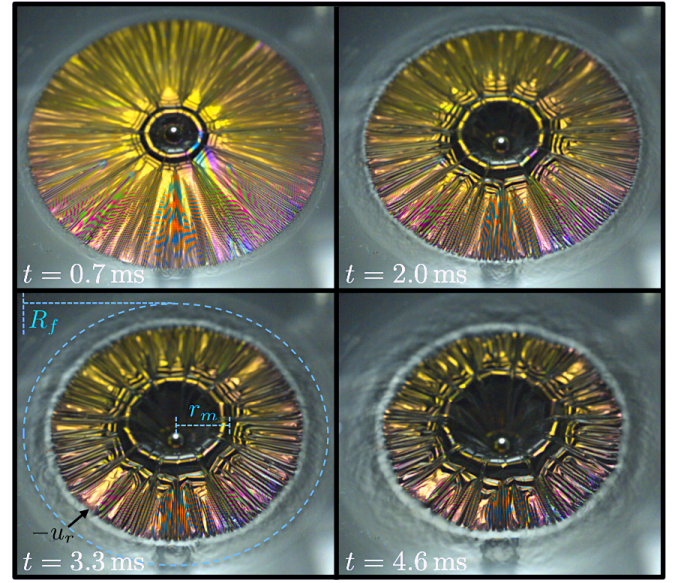


FIG. 1. A steel sphere (radius $R_s = 1.25$ mm) impacts a Polystyrene (PS) sheet (thickness $h = 350$ nm, radius $R_f = 17.15$ mm, floating at a water–air interface) at speed $V = 0.72$ m s^{−1}. A transverse wave propagates radially outwards from the point of impact, drawing the outer edge of the sheet inwards by a distance $u_r(R_f)$. The number of radial wrinkles in the sheet decreases with time (increasing impact depth Vt), in contrast to the static loading of a floating sheet [10, 15].

arguments. Here, we explore similar impact phenomena in thinner, stiffer sheets and, in doing so, uncover novel dynamic behaviour.

We investigate dynamic impact on ultra-thin polymer sheets subject to an applied background stress (provided by surface tension), see fig. 1 and Supplementary Movie 1 [26]. Polystyrene (PS) sheets of thickness 150 nm $\leq h \leq 530$ nm, Young's modulus $E = 3.46$ GPa and Poisson's ratio $\nu \approx 0.33$ were created by spin coating a PS-in-toluene solution onto glass slides [4]. The resulting sheets were cut to have radii 5.5 mm $\leq R_f \leq 22.7$ mm and

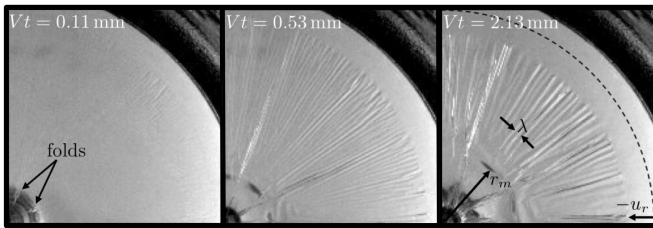


FIG. 2. Time series of one quadrant of a sheet ($h = 450$ nm, $R_f = 17.40$ mm) impacted by a sphere (radius $R_s = 1.75$ mm, $V = 1.17$ ms $^{-1}$) and imaged from below. The early onset of folds is apparent in the images, as is the propagation of a transverse wave (visible at radius r_m) and the coarsening of the radial wrinkles (increase of the wavelength λ). The initial position of the sheet edge is shown as the dashed circle, illustrating the retraction of the edge.

floated on water, with surface tension $\gamma_{lv} = 73$ mN m $^{-1}$ and density $\rho \approx 1000$ kg m $^{-3}$ [35]. Steel spheres, of radii 0.5 mm $\leq R_s \leq 5.0$ mm and density $\rho_s = 7720$ kg m $^{-3}$ were used as impactors; positioned above the centre of the sheet in a guiding tube (to ensure that the impact occurred vertically) and released using an electromagnet. The impact and resulting sheet deformation were imaged from below using a high-speed camera. The impact speed 0.6 ms $^{-1} \lesssim V \leq 2$ ms $^{-1}$ was measured by imaging the fall of the sphere from the side. Here, we focus on the deformation of the sheet that occurs at sufficiently early times that the velocity of the sphere is not noticeably affected by impact [26].

The images of fig. 1 show two key dynamic features of impact. Firstly, the gross vertical deflection of the sheet (i.e. the shape on which the wrinkles are superimposed) takes the form of a radially propagating transverse wave. This wave is analogous to the ripple observed when a stone is dropped into a pond. Here, however, the location of the maximum is polygonal; to avoid changing the Gaussian curvature of the initially planar sheet, this portion of the wave front has a number of approximately cylindrical humps separated by folds. Secondly, wrinkles form in the region ahead of the transverse wave, and their wavelength gradually increases — the wrinkles coarsen — see figs 1 and 2. This is qualitatively different from static experiments [10], which show that wrinkles become finer with increasing sheet deformation. We note two additional departures from static behaviour: in static indentation experiments, wrinkles are initially confined to a narrow annulus [5, 12], and reach the edge at indentation depths ~ 300 μ m [16], while folds appear at depths ~ 600 μ m – 2 mm [10, 15]. Both of these features appear at impact depths smaller by an order of magnitude ($Vt \approx 100$ μ m) in our dynamic experiments (see fig. 2).

Quantitative results for the propagation of the transverse wave are shown in fig. 3. While the ripples created by dropping a stone into a pond are known to progress according to the inertia–capillary scaling $r_m \sim t^{2/3}$ [25, 32]

(see black crosses in fig. 3a) we see that in the presence of an ultra-thin elastic sheet, $r_m \sim t^{1/2}$ instead. This scaling is reminiscent of the impact of a sphere into a liquid in the absence of surface tension, for which the contact point between the liquid and solid $r_c \approx \sqrt{3}(R_s V t)^{1/2}$ [33, 34]. However, the behaviour observed here is distinct from this impact phenomenology since, for example, the experimentally-measured prefactor in the scaling is dependent on the sheet radius R_f (see inset of fig. 3a). To explain this scaling, we consider the behaviour at very early times, when vertical deflections are small and the effect of gravity on the fluid may be neglected. Since the fluid is initially at rest and the impact is fast (the Reynolds number $\text{Re} = \rho V R_s / \mu \sim 10^3$), we assume that the fluid velocity $\mathbf{u} = \nabla \varphi$ for some velocity potential φ . The speed of sound in both the solid and liquid $\approx O(10^3)$ ms $^{-1}$, so on time scales $t \geq t_{\text{sound}} = R_f / c \approx 10$ μ s the fluid is incompressible and

$$\nabla^2 \varphi = 0. \quad (1)$$

At the deformed interface $z = w(r, t)$, we impose a kinematic condition

$$\frac{\partial \varphi}{\partial z} = \frac{\partial w}{\partial t} + \frac{\partial \varphi}{\partial r} \frac{\partial w}{\partial r}, \quad (2)$$

together with a dynamic boundary condition relating the stresses σ_{rr} and $\sigma_{\theta\theta}$ in the sheet to the pressure on the interface $p[r, w(r, t), t]$ via the membrane equation

$$p = -\sigma_{rr} \frac{\partial^2 w}{\partial r^2} - \sigma_{\theta\theta} \frac{1}{r} \frac{\partial w}{\partial r}. \quad (3)$$

The pressure p is, in turn, related to the velocity potential φ through Bernoulli's equation

$$\rho \left(\frac{\partial \varphi}{\partial t} + \frac{1}{2} |\nabla \varphi|^2 \right) + p = 0. \quad (4)$$

In writing (3) we have neglected the bending stiffness of the sheet over the lengthscale of the transverse wave (although we note that it is important in selecting the wrinkle wavelength), and we have also neglected the inertia of the sheet. Both approximations are justified in the derivation of a more detailed model [31].

To progress further, we note that the PS sheets used in our experiments are highly bendable [9, 10, 12] and so cannot sustain substantial compressive stresses. Instead, wrinkles form very early on, relaxing the compressive hoop stress so that $|\sigma_{\theta\theta}| \ll \sigma_{rr}$. Our experiments focus on times $t \geq t_{\text{sound}}$, for which in-plane stresses are in equilibrium, and so $\sigma_{rr} \approx \gamma_{lv} R_f / r$ [9, 12] (distinguishing our experiments from ref. [25] where $t \lesssim t_{\text{sound}}$). We present a detailed study of the resulting equations elsewhere [31], but focus here on a scaling approach: Laplace's equation (1) suggests that the vertical length scale over which the (infinite) bath of fluid feels the impact $z_* \sim r_m$. The kinematic and dynamic boundary conditions (2) and (3)–(4) respectively then suggest

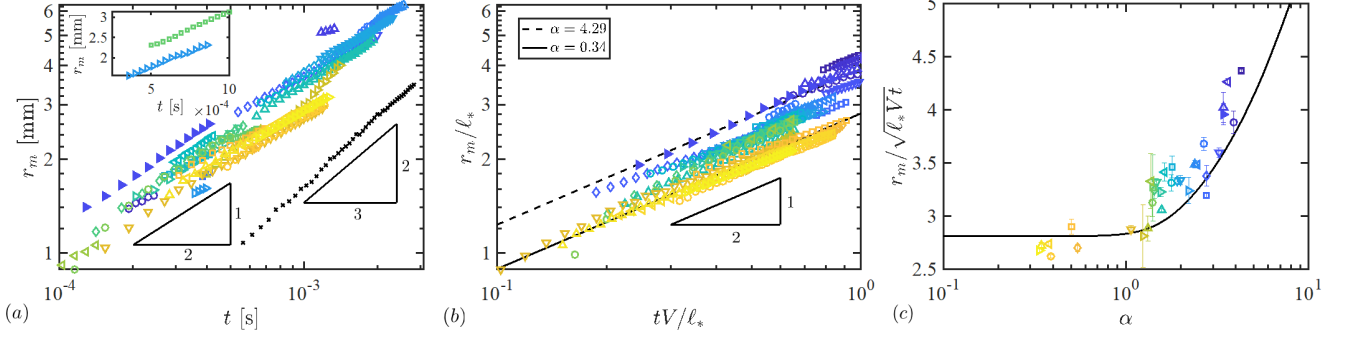


FIG. 3. The evolution of the transverse wave for a range of dimensionless sphere radii $\alpha = R_s/\ell_*$ in the range $0.34 \leq \alpha \leq 4.29$ (a) Measurements of the radial position of a capillary wave on a bare interface (\times) gives $r_m \sim t^{2/3}$, different from the behaviour with an ultra-thin PS sheet (coloured points). Inset: wave propagation depends on R_f ($= 5.51$ mm for \triangleleft and 13.30 mm for \circ). (b) Rescaling the data using the horizontal length scale $\ell_* = (\gamma_{lv} R_f / \rho V^2)^{1/2}$ and associated timescale $t_* = \ell_*/V$ shows that $r_m \sim (\ell_* V t)^{1/2}$, as in (5). The associated theoretical predictions (including prefactors) are shown for $\alpha = 0.34$ (solid line) and $\alpha = 4.29$ (dashed line). (c) The experimental prefactor $\beta = r_m / \sqrt{\ell_* V t}$ in (5) varies with α in a similar way to that predicted theoretically [31] (solid black line) at sufficiently early times (as defined in the SI). Throughout, data markers are colour coded according to the value of α in (c); experimental parameters are given in the SI.

that $\varphi_* \sim r_m V$ and $\varphi_* \sim \gamma_{lv} R_f V t^2 / (\rho r_m^3)$, respectively. Combining these scalings, we find that

$$r_m \sim \left(\frac{\gamma_{lv} R_f t^2}{\rho} \right)^{1/4}, \quad (5)$$

while the height of the wave scales with Vt . The typical curvature of the surface is $\kappa = Vt/r_m^2 \sim 1/\sqrt{\gamma R_f / \rho V^2}$, independent of t . Defining a lengthscale

$$\ell_* = \kappa^{-1} = \left(\frac{\gamma_{lv} R_f}{\rho V^2} \right)^{1/2}, \quad (6)$$

and time scale $t_* = \ell_*/V$, the scaling in (5) becomes $r_m/\ell_* = \beta(t/t_*)^{1/2}$, with some dimensionless prefactor β . We emphasize that the predicted scaling $r_m \sim t^{1/2}$ derives from the spatially-varying stress $\sigma_{rr} \sim 1/r$ and requires the sheet to be highly wrinkled with the stresses in equilibrium. While the data in fig. 3b confirms the scaling $r_m/\ell_* \sim (t/t_*)^{1/2}$ it does not collapse onto a single line; a more detailed analysis [31] shows that the prefactor β depends on the dimensionless sphere radius $\alpha = R_s/\ell_*$, in agreement with our data (fig. 3c).

While the impacted sheet might be expected to stretch, in fact $\gamma/(Eh) \sim 10^{-4} \ll 1$ so that the sheets are effectively inextensible. This preserves the length of radial lines (i.e. the radial strain $\epsilon_{rr} \approx 0$) so that the edge retraction follows directly from the vertical deflection, $-u_r(R_f) \sim \int_0^{R_f} (\partial w / \partial r)^2 dr \sim (Vt)^2 / r_m$, which from (5) yields

$$-u_r(R_f) \sim V^2 \left(\frac{\rho}{\gamma R_f} \right)^{1/4} t^{3/2}. \quad (7)$$

This scaling prediction is confirmed by experimental data (fig. 4a) though, again, the prefactor in (7) depends on

the dimensionless sphere radius α and can be predicted from a detailed analysis [31]. We note that our assumption of inextensibility (and hence the calculation of radial retraction) is only valid because the dominant tension arises from capillarity, in contrast to the dynamic indentation experiments of [25] where impact induces significant stretching of the sheet.

The radial retraction of the sheet $u_r(t)$ yields an excess length of material that is accommodated through wrinkling. We observe that the wavelength $\lambda(t)$ of these wrinkles increases in time (see fig. 4b) or, equivalently, the number of wrinkles decreases. To understand wrinkle formation and coarsening, we consider a material circle in the flat portion of the sheet, ahead of the transverse wavefront. We develop a simplified model by considering wrinkling in this material circle, driven by the compressive stress arising from radial retraction and moderated by the bending stiffness $B = Eh^3/[12(1-\nu^2)]$ of the sheet and the inertia of the underlying fluid. We focus on large radial positions only, so that the curvature of the sheet (associated with the transverse wave) may be neglected, and $r \gg \lambda$. We emphasize that the previously neglected bending stiffness of the sheet and compressive hoop stress must both be accounted for over the short lengthscale associated with wrinkling. We therefore model a freely floating 1D sheet which is subject to a compressive force $P(t)$ that mimics the compressive hoop stress $\sigma_{\theta\theta}(t)$, and evolves as a result of an imposed displacement of its ends $\Delta(t)$. The wrinkle coarsening is the result of the sheet being unable to move the liquid instantaneously, but, unlike previous studies [27, 28], here the fluid flow is inertial, not viscous.

We consider a sheet that lies along the x -axis and model its out-of-plane displacement, $w(x, t)$, using the beam equation subject to a linearized hydrodynamic

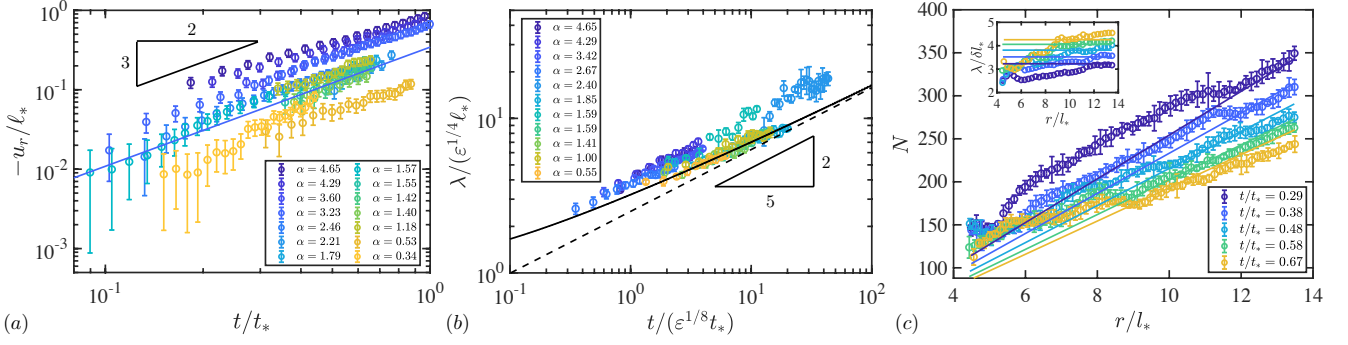


FIG. 4. The edge retraction and induced wrinkling of the sheet. (a) The sheet's edge moves radially by an amount $u_r(R_f) \sim t^{3/2}$, corresponding to approximate conservation of radial length (7). The solid line shows the theoretical prediction $-u_r(R_f)/\ell_* = 0.34(t/t_*)^{3/2}$, corresponding to $\alpha = 1.79$ (b) The mean wavelength λ of the radial wrinkles increases with time. The scaling is motivated by the existence of a short length scale $\epsilon^{1/4}\ell_*$ and fast timescale $\epsilon^{1/8}t_*$ in the asymptotic limit $\epsilon \rightarrow 0$ [31]; here $\epsilon = B/(\rho V^2 \ell_*^3) \approx 10^{-4}$ is a dynamic, inverse bendability [9]. The dashed black line illustrates the scaling (10), while the solid black curve shows numerical results [31]. λ was measured at $r(t) = 0.8[R_f - u_r(R_f, t)]$ by counting the number of wrinkles and averaging azimuthally [26]. (c) The number of wrinkles N increases approximately linearly with radial distance from the point of impact, corresponding to an instantaneous wavelength that is approximately uniform (inset). Data points show measurements at different times for $\alpha = 1.41$, while solid lines show the numerical predictions of a reduced one-dimensional model [31]. Experimental parameters for each figure are given in the SI.

pressure from (4). A balance between the bending stress, compressive stress and flow induced by wrinkling gives

$$-\rho \frac{\partial \varphi}{\partial t} = B \frac{\partial^4 w}{\partial x^4} + P(t) \frac{\partial^2 w}{\partial x^2}. \quad (8)$$

The compressive force $P(t)$ is not known *a priori*, and is determined by imposing a confinement

$$\int_{-\pi r}^{\pi r} \left(\frac{\partial w}{\partial x} \right)^2 dx = \Delta(t), \quad (9)$$

which expresses that the sheet wrinkles without changing its length. From a scaling point of view, the kinematic boundary condition gives $\partial \varphi / \partial z \sim \partial w / \partial t$. A scaling analysis of (8) then gives

$$\lambda \sim \left(\frac{B}{\rho} \right)^{1/5} t^{2/5}, \quad (10)$$

so that the wavelength is selected simply by a balance between bending stiffness and a 'dynamic substrate stiffness' associated with fluid inertia. The scaling (10) gives a reasonable account of our experimental data (see fig. 4b), although a detailed analysis ([31] and solid curve in fig. 4b) indicates that the power-law evolution of (10) may be modified by the geometric constraint (9), as occurs in a related problem [28].

We note that the radial position r and confinement $\Delta(t)$ enter only through (9); they therefore determine the amplitude of the wrinkles but not their wavelength. Experimentally, we observe that the number of wrinkles in a material circle increases approximately linearly with radial distance from the point of impact (fig. 4c), so that

the wavelength is approximately uniform in the outer region of the sheet at each instant (inset of fig. 4c). This breaks down in the inner region of the sheet where radial tension and curvature from the transverse wave provide additional stiffnesses [10].

We have studied the dynamic wrinkling of a thin elastic sheet floating on a liquid interface, highlighting several key features of this motion. In particular, the scaling $r_m \sim t^{1/2}$ illustrates the large change in the state of stress caused by highly developed wrinkling, while the evolution of the wrinkle pattern is very different to that observed statically [10, 12]: fluid inertia slows out-of-plane deformation of the sheet, selecting a dynamically evolving, but approximately uniform wrinkle wavelength. Finally, we ask when the wrinkle pattern is determined dynamically, rather than quasi-statically: for highly bendable sheets, the time scale over which wrinkles develop is much smaller than the time scale of the propagating wave [31] and so the requirement for dynamic wrinkle evolution is that $r_m \ll R_f$, i.e. $\delta = Vt \ll (\rho V^2 R_f^3 / \gamma)^{1/2} / \beta^2$.

This dynamic wrinkling may provide new means of controlling wrinkle patterns in a range of applications [6, 7]. Furthermore, the presence of a sheet also alters the dynamics of impact at later times: impact may ultimately submerge the sheet, or the sheet may rebound trapping the sphere at the interface. In both cases, the presence of the sheet may suppress the collapse of an air-filled cavity after impact and the subsequent formation of a Worthington jet [36] (see Supplementary Movie 2 [26]). Floating sheets could therefore find application as simple but effective anti-splash devices [37, 38] in naval and aerospace engineering, as well as in industrial coating processes [39], much as they do in more quotidian

scenarios [26].

ACKNOWLEDGMENTS

The research leading to these results has received funding from the European Research Council under the Eu-

ropean Union's Horizon 2020 Programme / ERC Grant Agreement no. 637334 (DV), the Royal Society (AAC-P) and the OUP John Fell Fund. The authors would like to thank Pedro Reis for helpful comments.

-
- [1] Y. W. Wong and S. Pellegrino, *J. Mech. Mater. Struct.* **1**, 3 (2006).
 - [2] P. M. Reis, *J. App. Mech.* **82**, 111001 (2015).
 - [3] C. M. Stafford, C. Harrison, K. L. Beers, A. Karim, E. J. Amis, M. R. van Landingham, H.-C. Kim, W. Volksen, R. D. Miller, and E. E. Simonyi, *Nature Mat.* **3**, 545 (2004).
 - [4] J. Huang, M. Juskiewicz, W. H. de Jeu, E. Cerda, T. Emrick, N. Menon, and T. P. Russell, *Science* **317**, 650 (2007).
 - [5] M. M. Ripp, V. Démery, T. Zhang, and J. D. Paulsen, *arXiv*, 1804.02421 (2018).
 - [6] J. B. Kim, P. Kim, N. C. Pégard, S. J. Oh, C. R. Kagan, J. W. Fleischer, H. A. Stone, and Y.-L. Loo, *Nature Phot.* **6** (2012).
 - [7] F. A. Bayley, J. L. Liao, P. N. Stavrinou, A. Chiche, and J. T. Cabral, *Soft Matter* **10**, 1155 (2014).
 - [8] E. Cerda and L. Mahadevan, *Phys. Rev. Lett.* **90**, 074302 (2003).
 - [9] B. Davidovitch, R. D. Schroll, D. Vella, M. Adda-Bedia, and E. Cerda, *Proc. Natl. Acad. Sci. USA* **108**, 18227 (2011).
 - [10] J. D. Paulsen, E. Hohlfield, H. King, J. Huang, Z. Qiu, T. P. Russell, N. Menon, D. Vella, and B. Davidovitch, *Proc. Natl. Acad. Sci.* **113**, 1144 (2016).
 - [11] P. Bella and R. Kohn, *J. Nonlinear Sci.* **24**, 1147 (2014).
 - [12] D. Vella, J. Huang, N. Menon, T. P. Russell, and B. Davidovitch, *Phys. Rev. Lett.* **114**, 014301 (2015).
 - [13] D. Vella, H. Ebrahimi, A. Vaziri, and B. Davidovitch, *Europhys. Lett.* **112**, 24007 (2015).
 - [14] J. D. Paulsen, V. Démery, C. D. Santangelo, T. P. Russell, B. Davidovitch, and N. Menon, *Nat. Mater.* **14**, 1206 (2015).
 - [15] D. P. Holmes and A. J. Crosby, *Phys. Rev. Lett.* **105**, 038303 (2010).
 - [16] D. Vella and B. Davidovitch, *Phys. Rev. E* **98**, 013003 (2018).
 - [17] H. Vandeparre, S. Gabrielle, F. Brau, C. Gay, K. K. Parker, and P. Damman, *Soft Matt.* **6**, 5751 (2010).
 - [18] F. Box, R. Bowman, and T. Mullin, *App. Phys. Lett.* **103**, 151909 (2013).
 - [19] S. Srinivasan, Z. Wei, and L. Mahadevan, *Phys. Rev. Fluids* **2**, 074103 (2017).
 - [20] D. O'Kiely, *Mathematical models for the glass sheet re-draw process*, Ph.D. thesis, University of Oxford (2017).
 - [21] J. R. Gladden, N. Z. Handzy, A. Belmonte, and E. Villermaux, *Phys. Rev. Lett.* **94**, 035503 (2005).
 - [22] R. Vermorel, N. Vandenberghe, and E. Villermaux, *Proc. Roy. Soc. A* **463**, 641 (2007).
 - [23] R. Vermorel, N. Vandenberghe, and E. Villermaux, *Proc. Roy. Soc. A* **465**, 823 (2009).
 - [24] L. Duchemin and N. Vandenberghe, *J. Fluid Mech.* **756**, 544 (2014).
 - [25] N. Vandenberghe and L. Duchemin, *Phys. Rev. E* **93**, 052801 (2016).
 - [26] See Supplementary Information for further details of the experimental procedure and image processing techniques as well as information about the Supplementary Movies.
 - [27] J. Chopin, M. Dasgupta, and A. Kudrolli, *Phys. Rev. Lett.* **119**, 088001 (2017).
 - [28] O. Kodio, I. M. Griffiths, and D. Vella, *Phys. Rev. Fluids* **2**, 014202 (2017).
 - [29] L. Pocivavsek, R. Dellsy, A. Kern, S. Johnson, B. H. Lin, K. Y. C. Lee, and E. Cerda, *Science* **320**, 912 (2008).
 - [30] H. Diamant and T. A. Witten, *Phys. Rev. Lett.* **107**, 164302 (2011).
 - [31] D. O'Kiely, F. Box, O. Kodio, J. P. Whiteley, and D. Vella, *arXiv* 1811.11288 (2018).
 - [32] J. B. Keller and M. J. Miksis, *SIAM J. Appl. Math.* **43**, 268 (1983).
 - [33] H. Wagner, *Zeit. Angew. Math. Mech.* **12**, 193 (1932).
 - [34] J. Philippi, P.-Y. Lagrée, and A. Antkowiak, *J. Fluid Mech.* **795**, 96 (2016).
 - [35] One experiment was performed with a water-glycerol mix with $\gamma_{lv} = 68 \text{ mN m}^{-1}$, $\rho \approx 1130 \text{ kg m}^{-3}$ and viscosity $\mu = 13 \text{ mPas}$ to assess the effect of liquid viscosity.
 - [36] A. M. Worthington, *A Study of Splashes* (Longmans, Green and Co., London, 1908).
 - [37] R. E. Pepper, L. Courbin, and H. A. Stone, *Phys. Fluids* **20**, 082103 (2008).
 - [38] C. J. Howland, A. Antkowiak, J. R. Castrejón-Pita, S. D. Howison, J. M. Oliver, R. W. Style, and A. A. Castrejón-Pita, *Phys. Rev. Lett.* **117**, 184502 (2016).
 - [39] D. Kumar, J. D. Paulsen, T. P. Russell, and N. Menon, *Science* **359**, 775 (2018).
 - [40] D. Sandlin, *Poop Splash Elimination*, SmarterEveryDay 22, (2011).